Studies of granularity of a hadronic calorimeter for tens-of-TeV jets at a 100 TeV pp collider

S.V. Chekanov[a], A.V. Kotwal[b,c], J. Proudfoot[a], S. Sen[b], N.V. Tran[c], S.-S. Yu[e], Chih-Hsiang Yeh[e]

[a] *HEP Division, Argonne National Laboratory, 9700 S. Cass Avenue, Argonne, IL 60439, USA.*
[b] *Department of Physics, Duke University, USA*
[c] *Fermi National Accelerator Laboratory*
[d] *Department of Physics, Michigan State University, 220 Trowbridge Road, East Lansing, MI 48824*
[e] *Department of Physics, National Central University, Chung-Li, Taoyuan City 32001, Taiwan*

Abstract

Texts

Keywords: multi-TeV physics, pp collider, future hadron colliders, FCC, SppC

1. Introduction

Particle collisions at energies beyond those attained at the LHC will lead to many challenges for detector technologies. Future experiments, such as high-energy LHC (HE-LHC), future circular pp colliders of the European initiative, FCC-hh [1] and the Chinese initiative, SppC [2] will be required to measure high-momentum bosons (W, Z, H) and top quarks with strongly collimated decay products that form jets. Studies of jet substructure can help identify such particles.

The reconstruction of jet substructure variables for collimated jets with transverse momentum above 10 TeV require an appropriate detector design. The most important for reconstruction of such jets are tracking and calorimeter. Recently, a number of studies [3, 4, 5] have been discussed using various fast simulation tools, such as Delphes [6], in which momenta of particles are smeared to mimic detector response.

A major step towards the usage of full Geant4 simulation to verify the granularity requirements for calorimeters was made in [7]. The studies included in this paper have illustrated a significant impact of granularity of electromagnetic (ECAL) and hadronic (HCAL) calorimeters on the shape of hadronic showers calculated using calorimeter hits for two particles separated by some angle. It was concluded that high granularity is essential in resolving two close-by particles for energies above 100 GeV.

This paper makes another step in understanding understanding of this problem in terms of high-level physics quantities typically used in physics analyses. Similar to the studies presented in [7], this paper is based on full Geant4 simulation with realistic jet reconstruction.

2. Simulation of detector response and event reconstruction

The description of the detector and software used for this paper is discussed in [7]. We use the SiFCC detector geometry with a software package that represents a versatile environment for simulations of detector performance, testing new technology options, event reconstruction techniques for future 100 TeV colliders.

The GEANT4 (version 10.3) [8] simulation of calorimeter response was complemented with the full reconstruction of calorimeter clusters formed by the Pandora algorithm [9, 10]. Calorimeter clusters were built from calorimeter hits in the ECAL and HCAL after applying the corresponding sampling fractions. No other corrections are applied. Hadronic jets were reconstructed with the FASTJET package [11] using the anti-k_T algorithm [12] with a distance parameter of 0.5.

In the following discussion, we use the simulations of a heavy Z' boson, a hypothetical gauge boson that arises from extensions of the electroweak symmetry of the Standard Model. The Z' bosons were simulated with the masses, $M = 5$, 10, 20 and 40 TeV. The lowest value represents a typical mass that is within the reach of the LHC experiments. The value 40 TeV represents the physics reach of 100 TeV colliders. The Z' particles are forced to decay to to two light-flavor jets ($q\bar{q}$), W^+W^- or $t\bar{t}$, where W and t decay hadronically. In all such scenarios, two highly boosted jets are produced, which are typically back-to-back in the laboratory frame. Typical transverse momenta of such jets are $\simeq M/2$. The main difference between considered decay types lays in different jet substructure. In the case of the $q\bar{q}$ decays, jets do not have any internal structure. In the case of W^+W^-, each jet originates from W, thus it has two subjects because of the decay $W \rightarrow q\bar{q}$. In the case of hadronic top decays, jets have three subjects due to the decay $t \rightarrow W^+ b \rightarrow q\bar{q}b$ The signal events were generated using the PYTHIA8generator with the default settings, ignoring interference with SM processes. The event samples used in this paper are available from the HepSim database [13].

3. Studies of jet properties

First let us consider several variables that represent jet substructure using different types of calorimeter granularity. The question we want to answer is how close the reconstructed jet substructure variables to the input "truth" value that are reconstructed using input particles directly from the PYTHIA8generator.

The effective radius is the average of the energy weighted radial distance in $\eta - \phi$ space of jet constituents. Recently, it has been studied for multi-TeV jets in Ref.[14].

Let us study the effect of granularity on jet splitting scales. A jet k_T splitting scale [15] is defined as a distance measure used to form jets by the k_T recombination algorithm [16, 17]. This has been studied by ATLAS [18], and more recently in the context of 100 TeV physics [14]. The distribution of the splitting scale $\sqrt{d_{12}} = \min(p_T^1, p_T^2) \times \delta R_{12}$ [18] at the final stage of the k_T clustering, where two subjets are merged into the final one, is shown in Fig. 2.
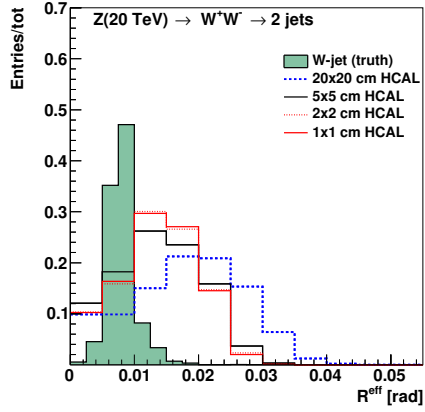
3.1. Jet subjettiness

We recall that N-subjettiness [? 19], τ_N, of jets has been proposed as a class of variables with which to study the decay products of a heavy particle inside jets. τ_N is
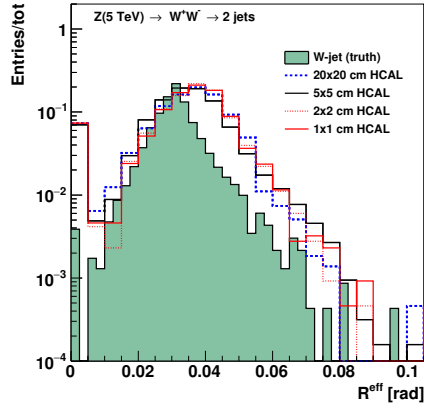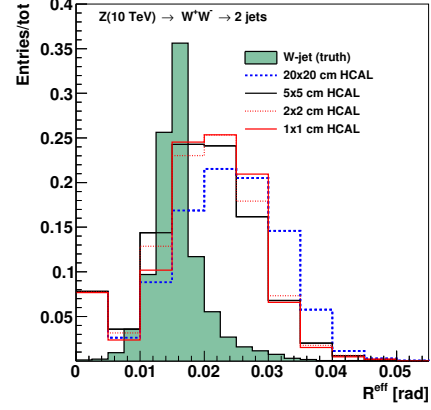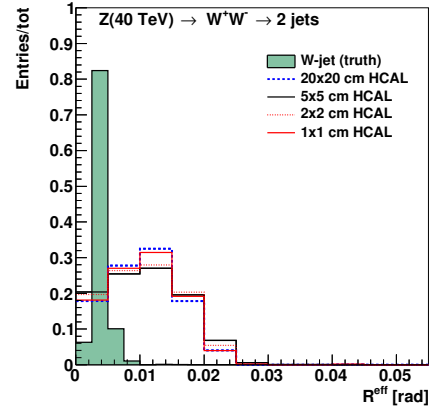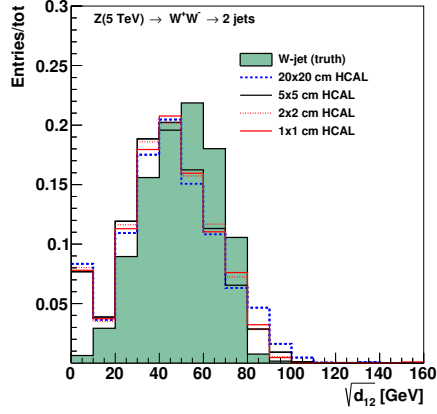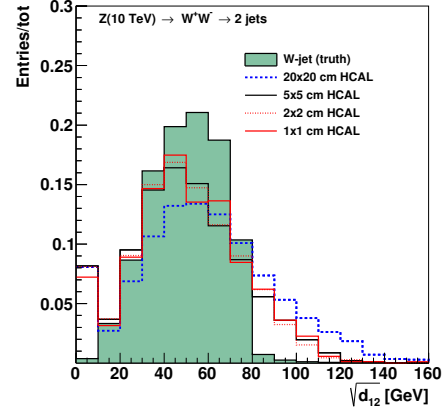
(a) 5 TeV
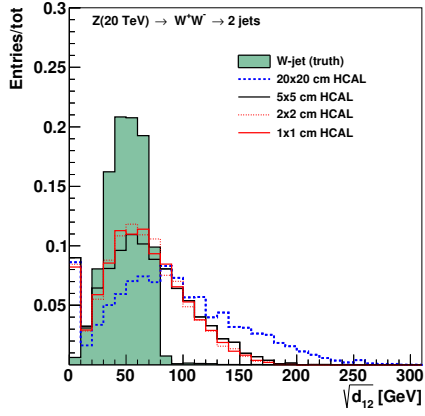
(b) 10 TeV

(c) 20 TeV

(d) 40 TeV

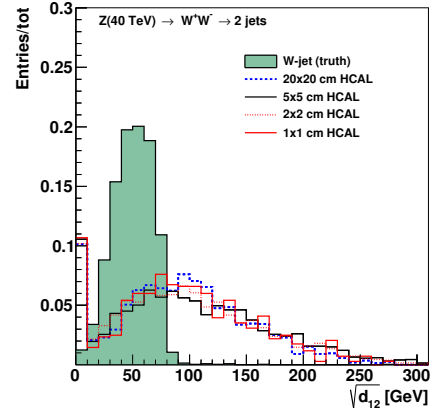Figure 1: Jet effective radius for different jet transverse moment and HCAL granularity.

(a) 5 TeV

(b) 10 TeV

(c) 20 TeV

(d) 40 TeV

Figure 2: Jet splitting scale for different jet transverse moment and HCAL granularity.

4

a measure of the degree to which a jet can be considered as being composed of N k_T-subjets [19]. The variable τ_{32}, defined as the ratio of the N-subjettiness variables τ_3/τ_2, is particularly sensitive to hadronically-decaying top-quark initiated jets. The variable, $\tau_{21} \equiv \tau_2/\tau_1$ can be used to reject background from W/Z decays. These variables do not strongly correlate with jet mass and can provide an independent check for the presence of top quarks. The jet substructure variables were obtained by re-running the k_T algorithm over the jet constituents of anti-k_T jets.

4. Soft drop in future collider performance

In this section, we use the specific method, soft-drop, to study the performance of the detector with the different detector cell sizes and center-of-mass(c.m.) energies.

4.1. The technic of Soft-drop

Soft-drop(SD)[??], taking literally, is the technique that reserves the soft P_T of jets which is greater than the set threshold. The formula and the technique are as following:

$$\frac{min(P_{T1}, P_{T2})}{P_{T1} + P_{T2}} > Z_{cut}(\frac{\Delta R_{12}}{R_0})^\beta \tag{1}$$

P_{T1}, P_{T2} are P_T of the two jets. Z_{cut} is soft drop threshold. ΔR_{12} are the two jets distance on the η-ϕ plane. β is the angular exponent. R_0 is the characteristic radius with clustering.

1. First, Anti-kt(AK) algorithm is used to reconstruct jets.
2. Second, after reconstructing the AK4 jets, Cambridge-Aachen (C/A) algorithm is used to decluster the jets into two (C/A) jets.
3. Third, these two jets are compared with the formula 1. Two jets will be reserved when they pass the formula, otherwise, the softer jet of two jets will be removed.
4. Finally, loop the procedure from 1.to 3.until the jets can not be declusteded into two jets.

In our study, we compare $\beta = 0$ with $\beta = 2$ and observe their performance in the future detector. For $\beta = 0$, the selection only depends on the Z_{cut}. For $\beta = 2$, the selection depends on the angle of two declustering jets and Z_{cut}, it is infrared and collinear (IRC) safe. The paper of SD[??] refer to the detail of it.

4.2. Analysis method

First, start at the central value of the signal median bin's right boundary. Then, add the left and right bins symmetrically to extend the width and draw the Receiver Operating Characteristic(ROC) curves.

4.3. The results and conclusions

In the Figure[3][5][7][9], distributions of mass under SD at $\beta = 0$ and $\beta = 2$ with different c.m. energies and detector cell sizes are presented. Because different β and signal contain the different ranges of mass, we choose the different ranges in the histograms.

In the Figure [4][6][8][10], ROC curves are used to perform the study of comparing different parameters. The figures want to show which detector cell size has the best "background rejection" with different c.m. energies. In other words, which cell size has the best separation power to distinguish signal from background with different c.m. energies.

In the Figure [4], they show the ROC curves for WW signal at SD with $\beta = 0$ with different detector cell sizes and c.m. energies. These performances show that 5,10, 20 TeV have the best distinguish power with the smallest (1×1) detector cell sizes. Similar to the tt signal at same β in Figure[6], they have the best distinguish power at 10, 20 TeV with the smallest (1×1) detector cell sizes.

Oppositely, in the figure [8] and figure [10], these show the ROC curves for WW and tt signal at SD with $\beta = 2$. They show the same conclusions that all c.m. energies don't have any improvements with the smallest (1×1) detector cell sizes. Some of the ROC curves with the different detector cell sizes almost overlap, that means the performances of this three sizes are very similar. In addition, some of them have the best distinguish power with the bigger detector (5×5 or 20×20) cell size.

After this study, we find that SD with $\beta = 0$ has the better performance for distinguishing signal from background than $\beta = 2$. so we choose SD at $\beta = 0$ to be our mass cut and apply it in other jet substructure variables for the next step.

5. Studies of signal and background separation using jet substructure variables

In this section, we study different jet substructure variables and compare their ability to separate signal from background with different detector sizes and c.m. energy using Mann-Whitney U test and ROC curves.

By definition of Mann Whitney U test, if U value is close to 0.5, it means two distributions have similar compositions, and we can not distinguish them very well. On the other hand, if U value of two distributions are close to 0, it means both compositions of both distribution are much different from each other.

5.1. N-subjettiness

N-subjettiness[??] is the detection technique of jet substructure that is used to identify boosted hadronically-decaying objects under the high c.m. conditions. We use τ variable to distinguish the number of subjet in a fatjet to separate signal and background with different detector sizes and c.m. energy.
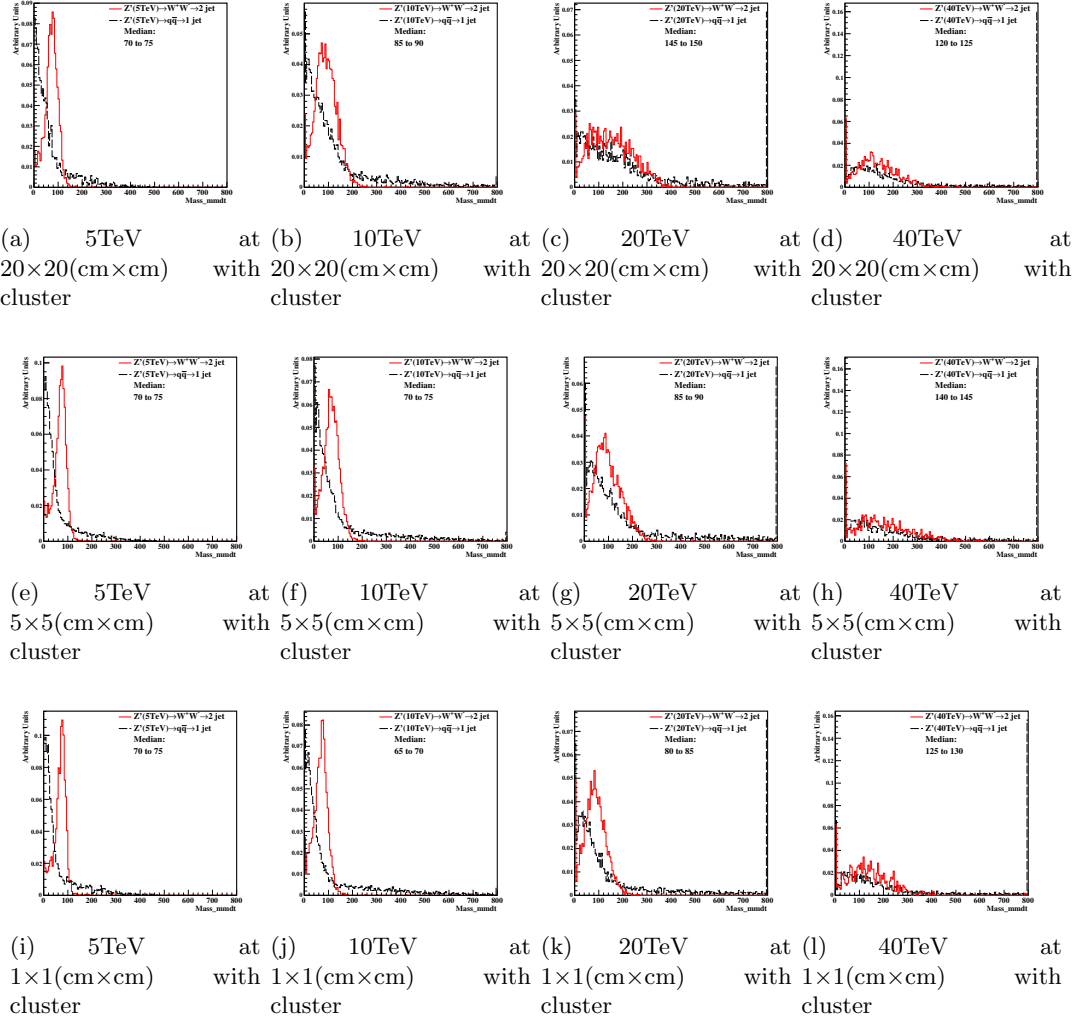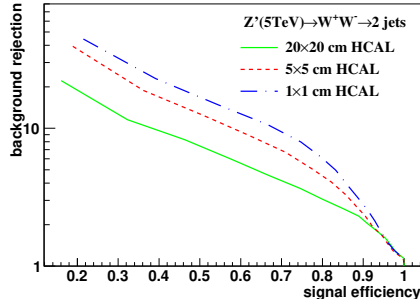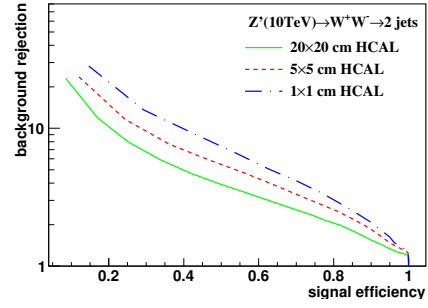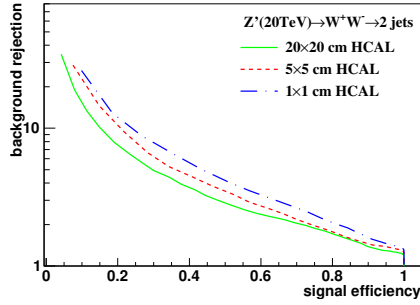
(a) 5TeV at 20×20(cm×cm) with cluster

(b) 10TeV at 20×20(cm×cm) with cluster

(c) 20TeV at 20×20(cm×cm) with cluster

(d) 40TeV at 20×20(cm×cm) with cluster

(e) 5TeV at 5×5(cm×cm) with cluster

(f) 10TeV at 5×5(cm×cm) with cluster

(g) 20TeV at 5×5(cm×cm) with cluster

(h) 40TeV at 5×5(cm×cm) with cluster

(i) 5TeV at 1×1(cm×cm) with cluster

(j) 10TeV at 1×1(cm×cm) with cluster

(k) 20TeV at 1×1(cm×cm) with cluster

(l) 40TeV at 1×1(cm×cm) with cluster

Figure 3: Distributions of mass soft drop at β=0, signal=ww, with 5,10,20,40TeV c.m. energy and different detector sizes. Cell Size in 20×20, 5×5, and 1×1(cm×cm) are shown here.
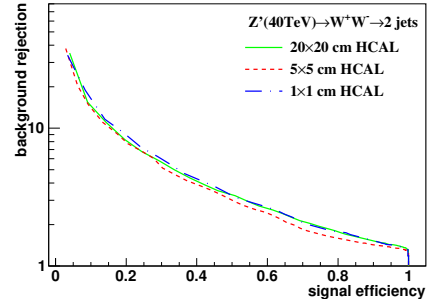
7

(a) Central at Median($20\times20=,5\times5=,1\times1=$) change width with cluster at 5TeV

(b) Central at Median($20\times20=,5\times5=,1\times1=$) change width with cluster at 10TeV

(c) Central at Median($20\times20=,5\times5=,1\times1=$) change width with cluster at 20TeV

(d) Central at Median($20\times20=,5\times5=,1\times1=$) change width with cluster at 40TeV

Figure 4: study of "fix central and change width" in mass soft drop at $\beta=0$, signal=ww, with 5, 10, 20, 40TeV c.m. energy and different detector sizes. Cell Size in 20×20, 5×5, and 1×1(cm$\times$cm) are shown in each picture.
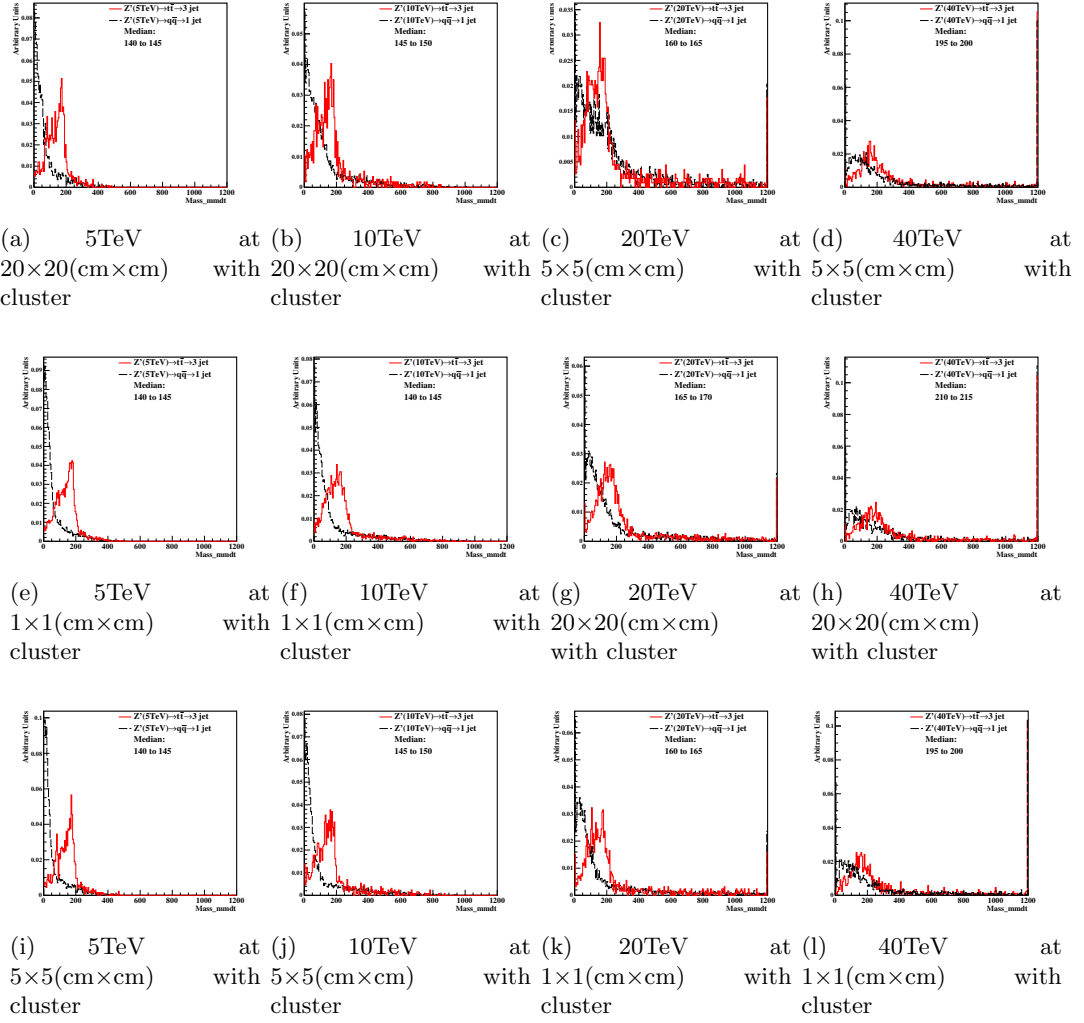
(a) 5TeV at 20×20(cm×cm) with cluster

(b) 10TeV at 20×20(cm×cm) with cluster

(c) 20TeV at 5×5(cm×cm) with cluster

(d) 40TeV at 5×5(cm×cm) with cluster

(e) 5TeV at 1×1(cm×cm) with cluster

(f) 10TeV at 1×1(cm×cm) with cluster

(g) 20TeV at 20×20(cm×cm) with cluster

(h) 40TeV at 20×20(cm×cm) with cluster

(i) 5TeV at 5×5(cm×cm) with cluster

(j) 10TeV at 5×5(cm×cm) with cluster

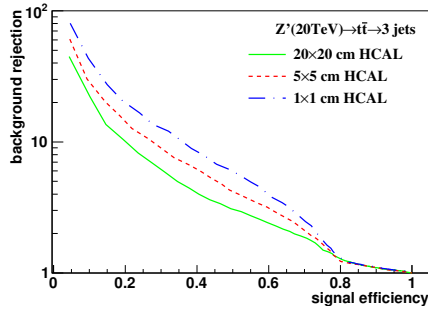(k) 20TeV at 1×1(cm×cm) with cluster

(l) 40TeV at 1×1(cm×cm) with cluster

Figure 5: Distributions of mass soft drop at β=0, signal=tt, with 5,10,20,40TeV c.m. energy and different detector sizes. Cell Size in 20×20, 5×5, and 1×1(cm×cm) are shown here.
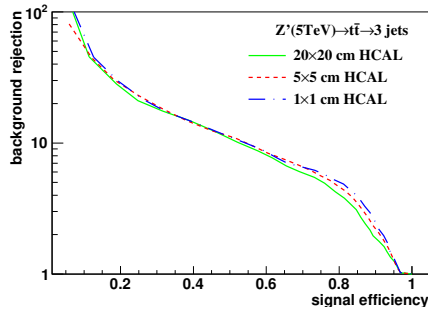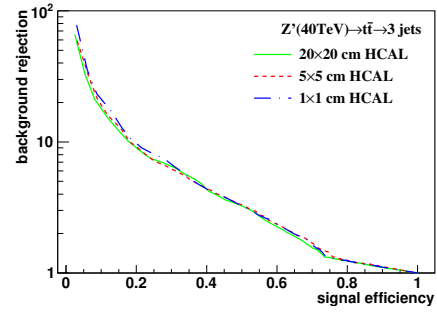
(a) Central at Median(20×20=,5×5=,1×1=) change width with cluster at 5TeV
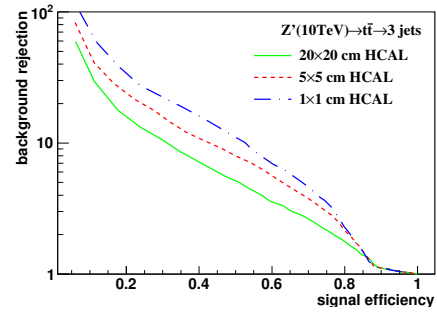
(b) Central at Median(20×20=,5×5=,1×1=) change width with cluster at 10TeV

(c) Central at Median(20×20=,5×5=,1×1=) change width with cluster at 20TeV

(d) Central at Median(20×20=,5×5=,1×1=) change width with cluster at 40TeV

Figure 6: study of "fix central and change width" in mass soft drop at β=0, signal=tt, with 5, 10, 20, 40TeV c.m. energy and different detector sizes. Cell Size in 20×20, 5×5, and 1×1(cm$\times$cm) are shown in each picture.

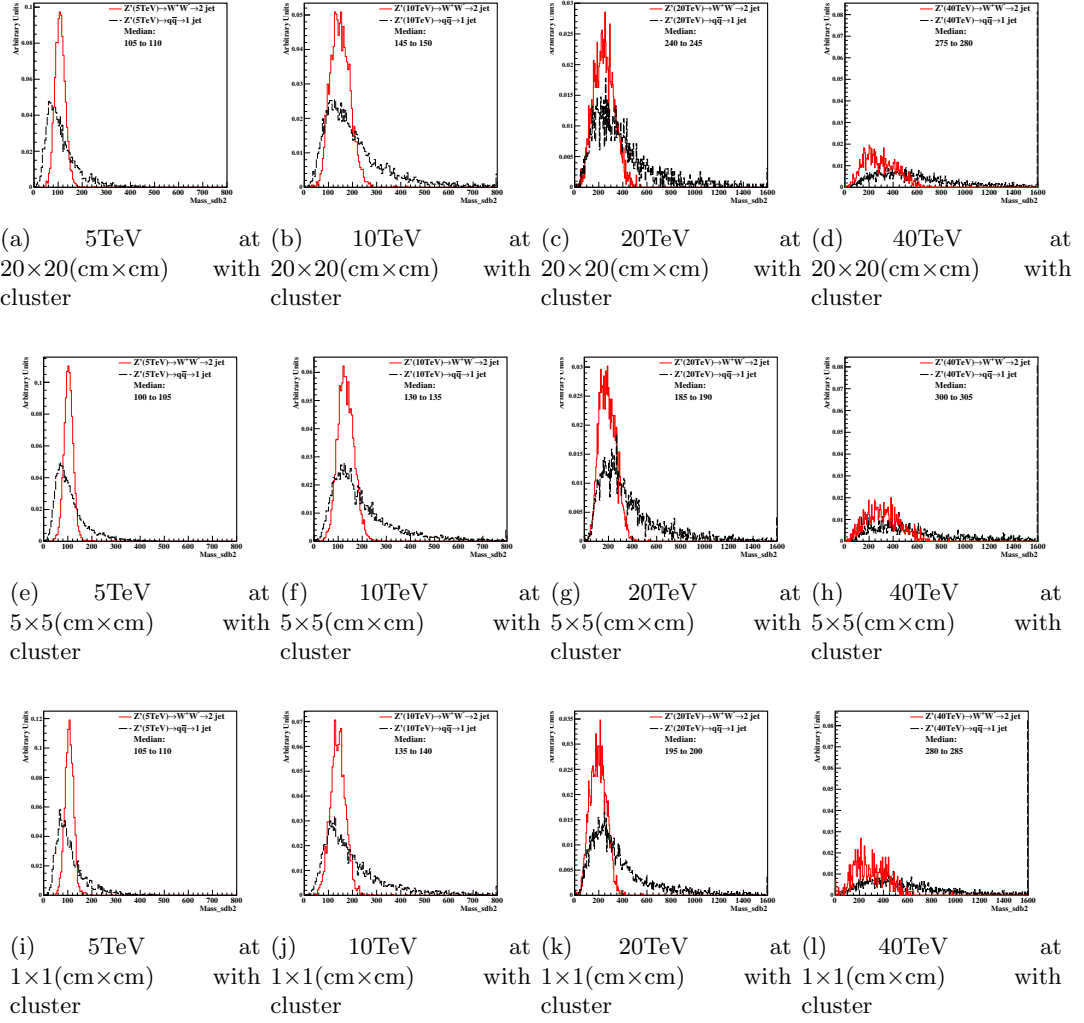(a) 5TeV at 20×20(cm×cm) with cluster

(b) 10TeV at 20×20(cm×cm) with cluster

(c) 20TeV at 20×20(cm×cm) with cluster

(d) 40TeV at 20×20(cm×cm) with cluster

(e) 5TeV at 5×5(cm×cm) with cluster

(f) 10TeV at 5×5(cm×cm) with cluster

(g) 20TeV at 5×5(cm×cm) with cluster

(h) 40TeV at 5×5(cm×cm) with cluster

(i) 5TeV at 1×1(cm×cm) with cluster

(j) 10TeV at 1×1(cm×cm) with cluster

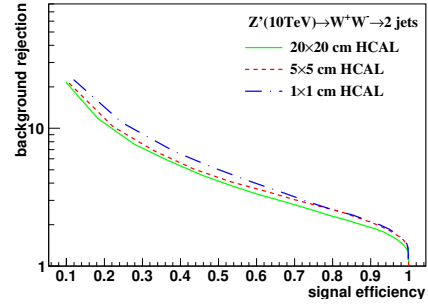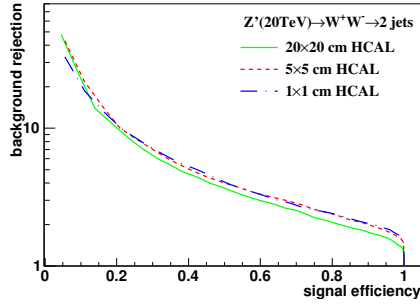(k) 20TeV at 1×1(cm×cm) with cluster

(l) 40TeV at 1×1(cm×cm) with cluster

Figure 7: Distributions of mass soft drop at β=2, signal=ww, with 5,10,20,40TeV c.m. energy and different detector sizes. Cell Size in 20×20, 5×5, and 1×1(cm×cm) are shown here.
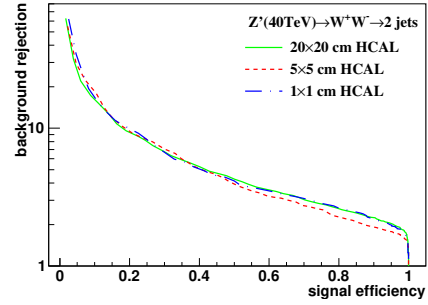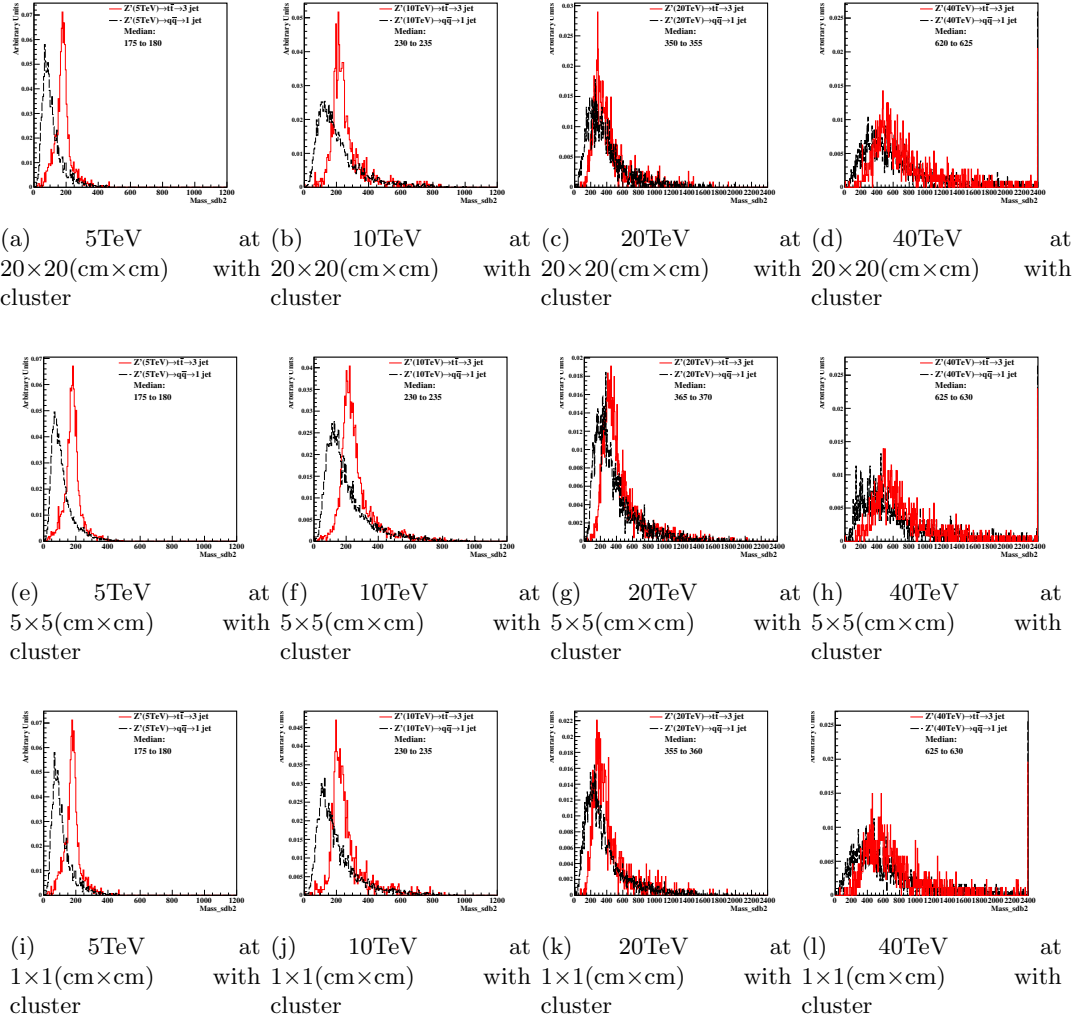
11
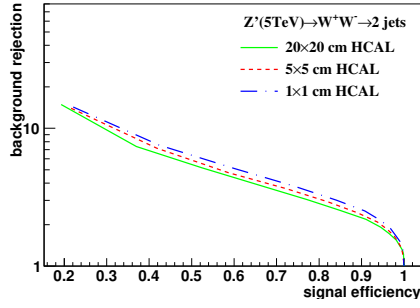
(a) Central at Median($20 \times 20 =, 5 \times 5 =, 1 \times 1 =$) change width with cluster at 5TeV

(b) Central at Median($20 \times 20 =, 5 \times 5 =, 1 \times 1 =$) change width with cluster at 10TeV

(c) Central at Median($20 \times 20 =, 5 \times 5 =, 1 \times 1 =$) change width with cluster at 20TeV

(d) Central at Median($20 \times 20 =, 5 \times 5 =, 1 \times 1 =$) change width with cluster at 40TeV

Figure 8: study of "fix central and change width" in mass soft drop at β=2, signal=ww, with 5, 10, 20, 40TeV c.m. energy and different detector sizes. Cell Size in 20×20, 5×5, and 1×1(cm×cm) are shown in each picture.

(a) 5TeV at 20×20(cm×cm) with cluster

(b) 10TeV at 20×20(cm×cm) with cluster

(c) 20TeV at 20×20(cm×cm) with cluster

(d) 40TeV at 20×20(cm×cm) with cluster

(e) 5TeV at 5×5(cm×cm) with cluster

(f) 10TeV at 5×5(cm×cm) with cluster

(g) 20TeV at 5×5(cm×cm) with cluster

(h) 40TeV at 5×5(cm×cm) with cluster

(i) 5TeV at 1×1(cm×cm) with cluster

(j) 10TeV at 1×1(cm×cm) with cluster

(k) 20TeV at 1×1(cm×cm) with cluster

(l) 40TeV at 1×1(cm×cm) with cluster
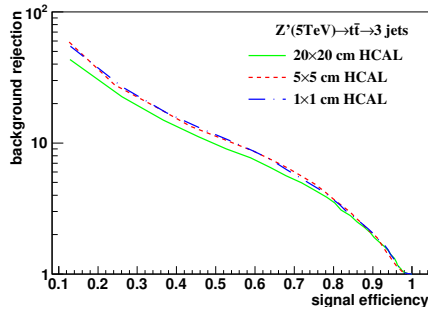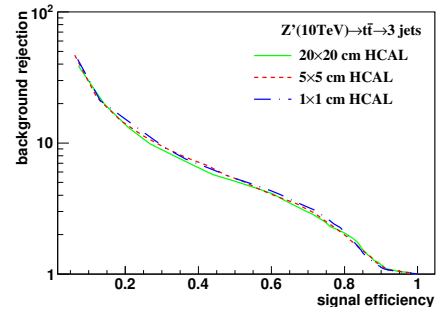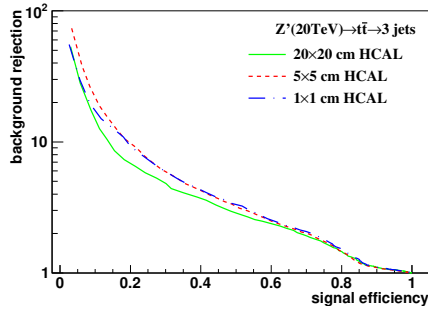
Figure 9: Distributions of mass soft drop at β=2, signal=tt, with 5,10,20,40TeV c.m. energy and different detector sizes. Cell Size in 20×20, 5×5, and 1×1(cm×cm) are shown here.
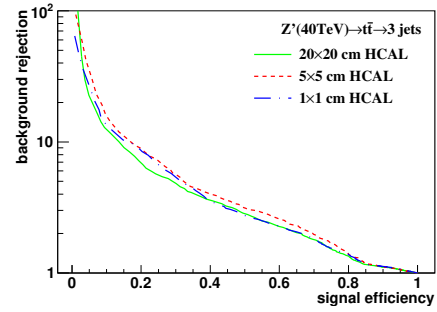
13

(a) Central at Median($20 \times 20=, 5 \times 5=, 1 \times 1=$) change width with cluster at 5TeV

(b) Central at Median($20 \times 20=, 5 \times 5=, 1 \times 1=$) change width with cluster at 10TeV

(c) Central at Median($20 \times 20=, 5 \times 5=, 1 \times 1=$) change width with cluster at 20TeV

(d) Central at Median($20 \times 20=, 5 \times 5=, 1 \times 1=$) change width with cluster at 40TeV

Figure 10: study of "fix central and change width" in mass soft drop at β=2, signal=tt, with 5, 10, 20, 40TeV c.m. energy and different detector sizes. Cell Size in 20×20, 5×5, and 1×1(cm$\times$cm) are shown in each picture.

14

5.1.1. The technic of N-subjettiness

The formula and the technique are as following:

$$\tau_N = \frac{1}{d_0} \sum_k p_{T,k} min\{\Delta R_{1,k}, \Delta R_{2,k}, ...\Delta R_{N,k}\} \tag{2}$$

$$d_0 = \sum_k p_{T,k} R_0 \tag{3}$$

k runs over all constituent particles in the given jets (fatjet), $p_{T,k}$ are their transverse momentum, $\Delta R_{J,k} = \sqrt{(\Delta \eta)^2 + (\Delta \phi)^2}$ is the distance between the constituent particles k and the candidate subjet J on the $\eta - \phi$ plane. R_0 is the characteristic jet radius used in Anti-kt(AK) jet algorithm at starting. d_0 is the normalization factor.

1. First, Anti-kt(AK) algorithm is used to reconstruct jets
2. Second, after reconstructing the AK4 jets, exclusive k_T algorithm[??] is used in finding the jet axis in a fatjet.
3. Third, start running formula [2] and loop all constituent particles in a fatjet.
4. Finally, when finishing running all particles, it will give out τ_N, where N is positive integer.

If a fatjet has N subjet(s)[??], its τ_N is smaller than the τ_N of the fatjet with different number of subjets. For example, if we compare the τ_2 of one-subjet fatjet and two-subjets one, two-subjets fatjet has smaller τ_2 than one-subjet one. On the other hand, one-subjet fatjet has smaller τ_1 than two-subjets one. In the end, we can use the ratio of τ_2 and τ_1 (τ_{21}) to distinguish fatjet with one-subjet case and-two subjets case.τ_{21} is used to discriminate the fatjet shape, and it can be modified with different number of subjet.

In our study, we use τ_{21} and τ_{32} in distinguishing two-subjets fatjet and three-subjets fatjet from one-subjet fatjet individually. We want to use this two ratio values to distinguish signal from background.

5.1.2. Analysis method

First, we select the events in mass window by using SD with $\beta = 0$ and 75% signal efficiency. Then, we find the highest ratio bin to be our seed bin. Next, we compare the left and right of ratio bin, and add the higher bin to be our width. Finally, We can use this width to draw the ROC curves.
2

5.1.3. The results and conclusion

In the figure [13][15], they show the histograms of τ_{21} and τ_{32} after selecting the events. In all figures, they also include the Mann-Whitney U value in ir the legend.

As a result of figure [14][16], they perform the ROC curves of τ_{21} and τ_{32} with different detector cell sizes and c.m. energy. The smallest detector cell (1×1) doesn't

have the best separation power to distinguish signal from background. Some of them have the best separation power with the bigger cell size (5×5 and 20×20).

In Figure [17](a)(b), they show the summary plots of τ_{21} and τ_{32} with the rawhit cut with 0.5GeV using Mann Whitney U test. In τ_{21}, 5TeV has better separation power when detector sizes get smaller. When energy increases, there is no improvement in the smallest detector cell size (1×1). In τ_{32}, the case is similar to τ_{21}. Even worse, with some c.m. energies, the bigger detector sizes (5×5 and 20×20) have better separation power than the smallest detector sizes (1×1).

5.2. Studies of signal and background separation using jet substurcture variable: Energy correlation function

Energy correlation function (ECF) [??] is another kind of detection technique of jet substurcture that is used to distinguish the number of subjets in a fatjet under high c.m. energy conditions. This method only uses the momenta of particles and the angles between them without additional algorithm.

5.2.1. The technic of energy correlation function

The basic ECF formula is as following:

$$ECF(N,\beta) = \sum_{i_1<i_2<....<i_N\in J}(\prod_{a=1}^{N} E_{ia})(\prod_{b=1}^{N-1}\prod_{c=b+1}^{N}\theta_{i_bi_c})^{\beta} \qquad (4)$$

In the formula 4, the sum loop all particles in the jet J, E are the energy of particles, and θ are the angles between the particles.

We apply two approximation. First, because under the high energy limitation $p >> m$, $E \approx p$. Second, we use Radius R between particles naturally, so our ECF formula (4) can be modified to the formula:

$$ECF(N,\beta) = \sum_{i_1<i_2<....<i_N\in J}(\prod_{a=1}^{N} P_{ia})(\prod_{b=1}^{N-1}\prod_{c=b+1}^{N}R_{i_bi_c})^{\beta} \qquad (5)$$

From the modified ECF formula (5), in order to use the dimensionless observation to determine whether the number of subjets in system, parameter τ_N is defined as:

$$\tau_N^{(\beta)} \equiv \frac{ECF(N+1,\beta)}{ECF(N,\beta)} \qquad (6)$$

The idea of formula (6) is from N-subjetness, because the behavior of it is very similar to N-subjetness as reference [??]. In general, if the system has N subjets, $ECF(N+1,\beta)$ should be significantly smaller than $ECF(N,\beta)$, so we can use this advantage to distinguish different number of subjets. FInally, because it is suggested to used τ_{21}, τ_{32} [??] to distinguish two-subjets fatjet and three-subjets fatjet from one-subjet fatjet, in the ECF, it also defines the ratio of τ there, and define the energy

correlation double ratio that is used in our study:

$$C_N^{(\beta)} \equiv \frac{\tau_N^{(\beta)}}{\tau_{N-1}^{(\beta)}} = \frac{ECF(N-1,\beta)ECF(N+1,\beta)}{ECF(N,\beta)^2} \tag{7}$$

We set N=2 and $\beta = 1$ (C_2^1) to distinguish two-subjets fatjet from one-subjet fatjet.

5.2.2. Analysis method

First, we select the events in mass window by using SD with $\beta = 0$ and 75% signal efficiency. Then, we find the highest ratio bin to be our seed bin. Next, we compare the left and right of ratio bin, and add the higher bin to be our width. Finally, We can use this width to draw the ROC curves.

5.2.3. The results and conclusion

In the figure [11], they show the histograms of τ_{21} and τ_{32} after selecting the events. In all figures, they also include the Mann-Whitney U value in their legend

As a result of figure [12], they perform the ROC curves of C_2^1 with different detector cell sizes and c.m. energy. The smallest detector cell (1×1) doesn't have the best separation power to distinguish signal from background. In addition, in some cases such like (a), the biggest one (20×20) has the best distinguish power under the same c.m. energy.

In Figure [17](c), it shows the summary plots with the rawhit cut with 0.5GeV using Mann Whitney U test. For conclusion, all separation power aren't improved by smallest cell size (1×1).

Acknowledgements

(a) 5TeV at 20×20(cm×cm) 0.5GeV

(b) 10TeV at in 20×20(cm×cm) 0.5GeV

(c) 20TeV at in 20×20(cm×cm) 0.5GeV

(d) 40TeV at in 20×20(cm×cm) in 0.5GeV

(e) 5TeV at 5×5(cm×cm) 0.5GeV

(f) 10TeV at in 5×5(cm×cm) 0.5GeV

(g) 20TeV at in 5×5(cm×cm) 0.5GeV

(h) 40TeV at in 5×5(cm×cm) in 0.5GeV

(i) 5TeV at 1×1(cm×cm) 0.5GeV

(j) 10TeV at in 1×1(cm×cm) 0.5GeV

(k) 20TeV at in 1×1(cm×cm) 0.5GeV
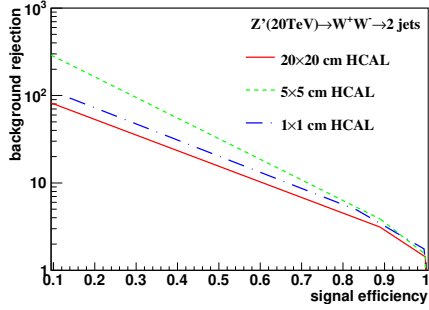
(l) 40TeV at in 1×1(cm×cm) in 0.5GeV

Figure 11: Distributions of Mann-Whitney value U in 5, 10, 20, 40TeV energy collision for c2b1 in different detector sizes. Cell Size in 20×20, 5×5, and 1×1(cm×cm) are shown here.
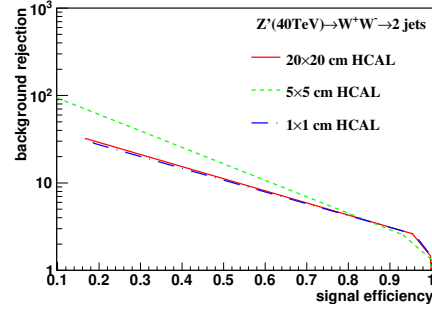
18

(a) 5 TeV using Rawhit 0.5GeV cut method with New2 after cut Method

(b) 10 TeV using Rawhit 0.5GeV cut method with New2 after cut Method

(c) 20 TeV using Rawhit 0.5GeV cut method with New2 after cut Method

(d) 40 TeV using Rawhit 0.5GeV cut method with New2 after cut Method

Figure 12: Signal efficiency versus background rejection rate using c2b1.The energies of collision at (a)5, (b)10, (c)20, (d)40TeV are shown here. In each picture, the three ROC curves correspond to different detector sizes.
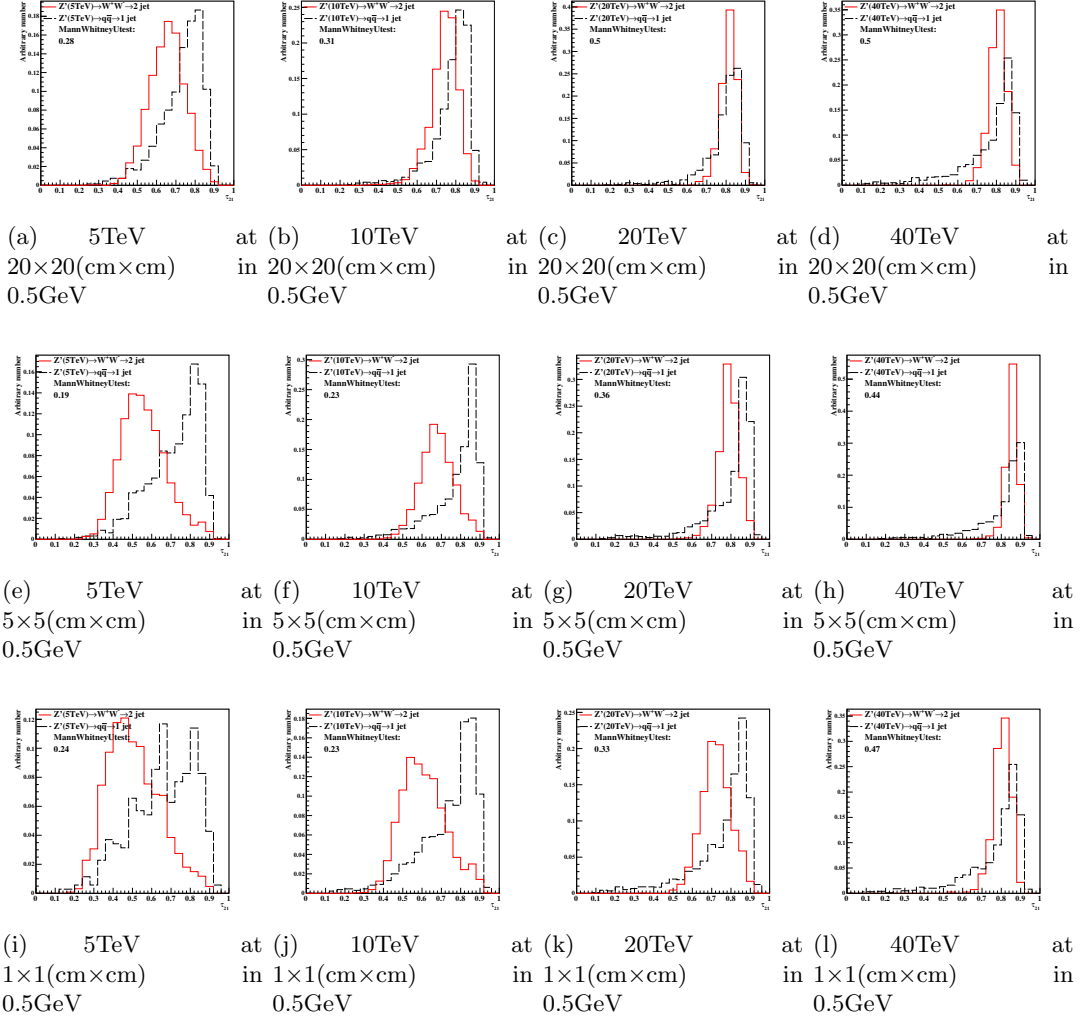
(a) 5TeV at 20×20(cm×cm) 0.5GeV

(b) 10TeV in 20×20(cm×cm) 0.5GeV

(c) 20TeV in 20×20(cm×cm) 0.5GeV

(d) 40TeV at in 20×20(cm×cm) 0.5GeV

(e) 5TeV at 5×5(cm×cm) 0.5GeV

(f) 10TeV in 5×5(cm×cm) 0.5GeV

(g) 20TeV in 5×5(cm×cm) 0.5GeV

(h) 40TeV at in 5×5(cm×cm) 0.5GeV

(i) 5TeV at 1×1(cm×cm) 0.5GeV

(j) 10TeV in 1×1(cm×cm) 0.5GeV

(k) 20TeV in 1×1(cm×cm) 0.5GeV

(l) 40TeV at in 1×1(cm×cm) 0.5GeV

Figure 13: Distributions of Mann-Whitney value U in 5, 10, 20, 40TeV energy collision for τ_{21} in different detector sizes. Cell Size in 20×20, 5×5, and 1×1(cm×cm) are shown here.
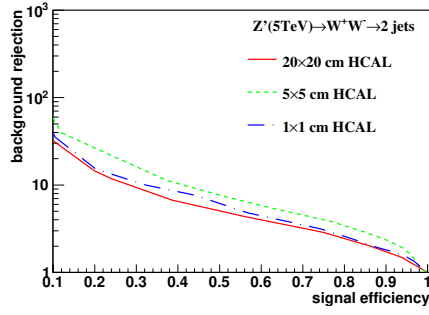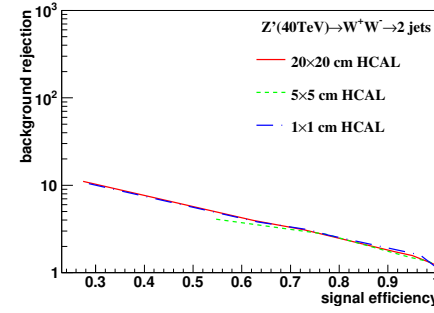
(a) 5 TeV using Rawhit 0.5GeV cut method with New2 after cut Method
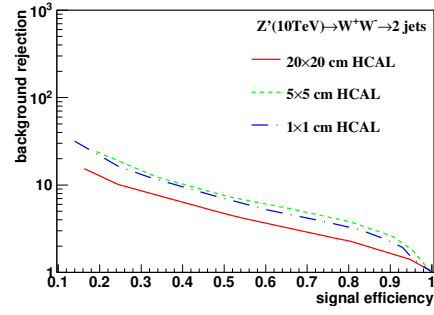
(b) 10 TeV using Rawhit 0.5GeV cut method with New2 after cut Method
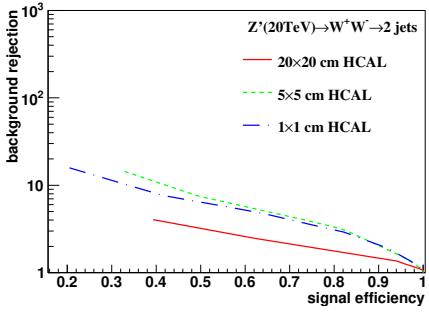
(c) 20 TeV using Rawhit 0.5GeV cut method with New2 after cut Method

(d) 40 TeV using Rawhit 0.5GeV cut method with New2 after cut Method

Figure 14: Signal efficiency versus background rejection rate using τ_{21}. The energies of collision at (a)5, (b)10, (c)20, (d)40TeV are shown here. In each picture, the three ROC curves correspond to different detector sizes.

(a) 5TeV at 20×20(cm×cm) 0.5GeV

(b) 10TeV at in 20×20(cm×cm) 0.5GeV

(c) 20TeV at in 20×20(cm×cm) 0.5GeV

(d) 40TeV at in 20×20(cm×cm) in 0.5GeV

(e) 5TeV at 5×5(cm×cm) 0.5GeV

(f) 10TeV at in 5×5(cm×cm) 0.5GeV

(g) 20TeV at in 5×5(cm×cm) 0.5GeV

(h) 40TeV at in 5×5(cm×cm) in 0.5GeV

(i) 5TeV at 1×1(cm×cm) 0.5GeV

(j) 10TeV at in 1×1(cm×cm) 0.5GeV

(k) 20TeV at in 1×1(cm×cm) 0.5GeV
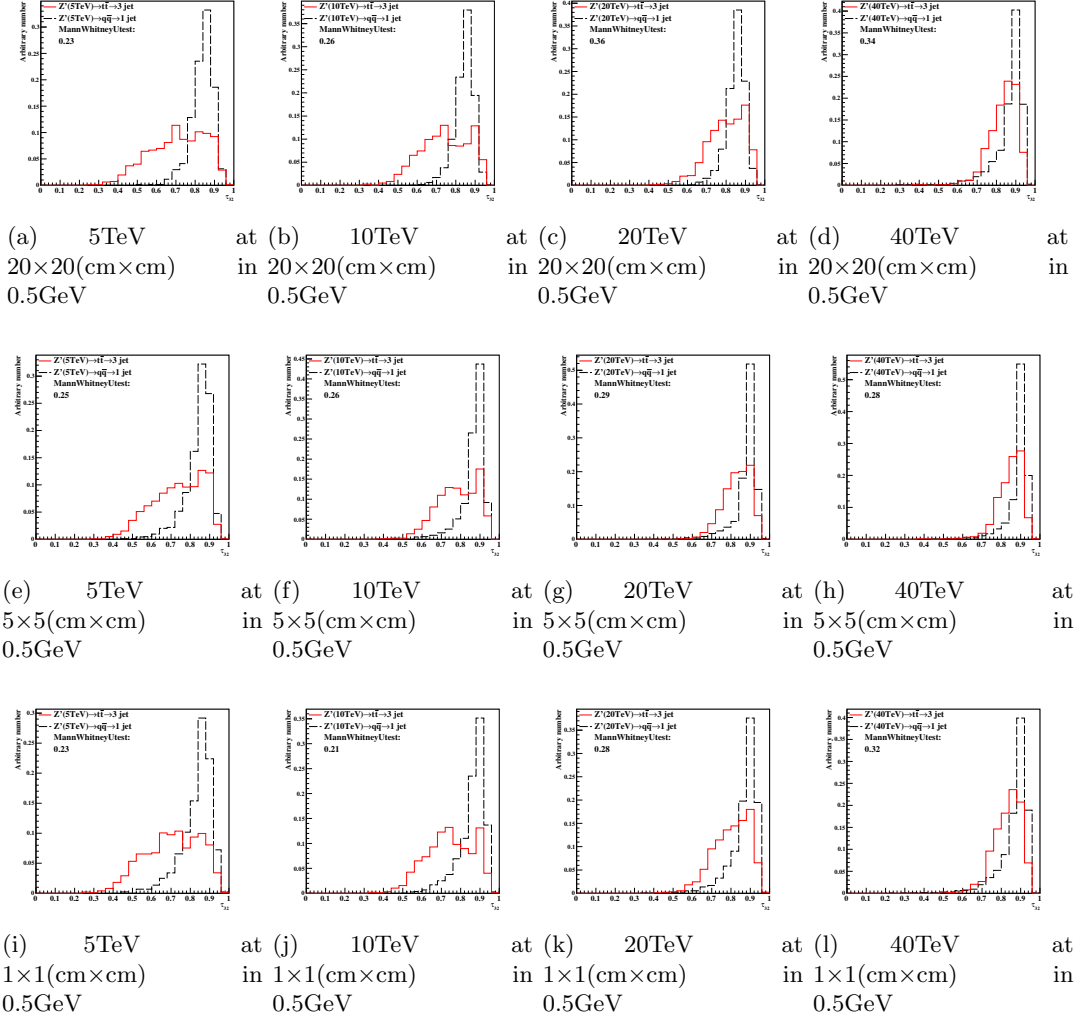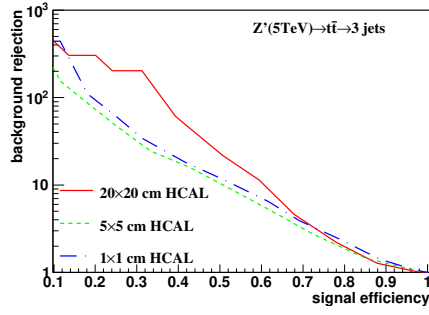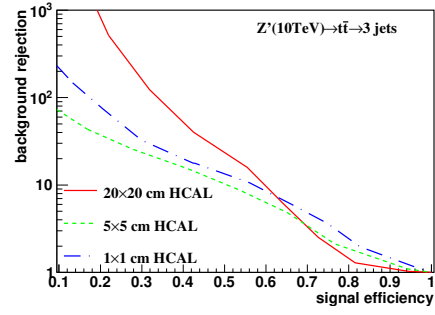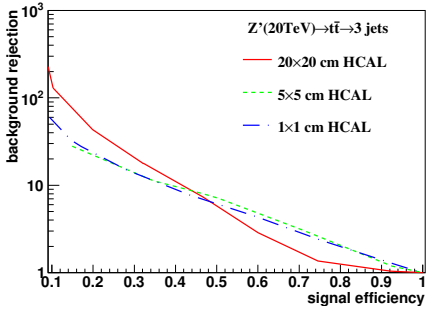
(l) 40TeV at in 1×1(cm×cm) in 0.5GeV

Figure 15: Distributions of Mann-Whitney value U in 5, 10, 20, 40TeV energy collision for τ_{32} in different detector sizes. Cell Size in 20×20, 5×5, and 1×1(cm×cm) are shown here.
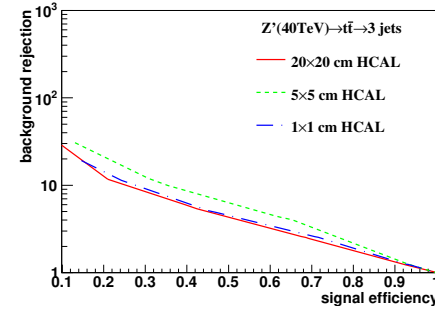
(a) 5 TeV using Rawhit 0.5GeV cut method with New2 after cut Method

(b) 10 TeV using Rawhit 0.5GeV cut method with New2 after cut Method
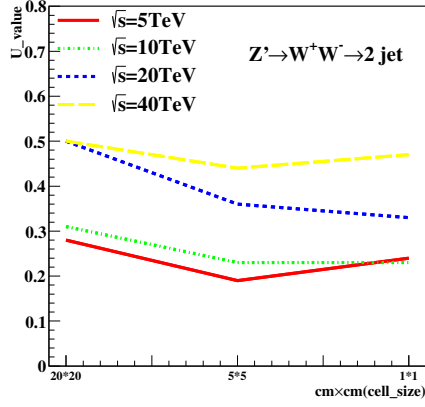
(c) 20 TeV using Rawhit 0.5GeV cut method with New2 after cut Method
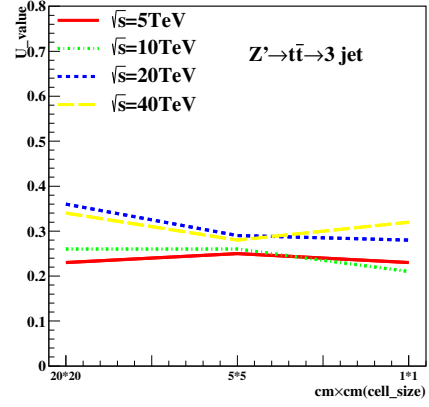
(d) 40 TeV using Rawhit 0.5GeV cut method with New2 after cut Method
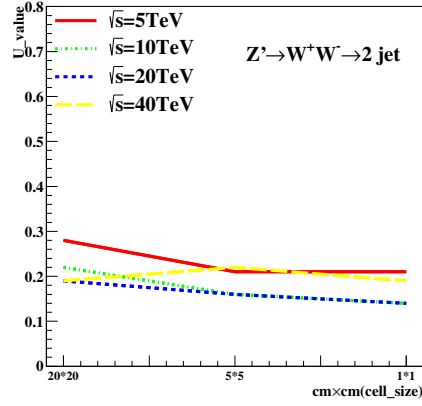
Figure 16: Signal efficiency versus background rejection rate using τ_{32}. The energies of collision at (a)5, (b)10, (c)20, (d)40TeV are shown here. In each picture, the three ROC curves correspond to different detector sizes.

23

(a) τ_{21} rawhit cut with 0.5GeV

(b) τ_{32} rawhit cut with 0.5GeV

(c) $c_2^{(1)}$ rawhit cut with 0.5GeV

Figure 17: The Mann-Whitney U values for τ_{21},τ_{32} and $c_2^{(1)}$ reconstructed from calorimeter hit at 05GeV cut with different collision energies correspond to different detector sizes in rawhit cut with 05GeV. The energies of collision at 5, 10, 20, 40, 20, 40TeV are shown in each figure.

References

[1] M. Benedikt, The Global Future Circular Colliders EffortCERN-ACC-SLIDES-2016-0016. Presented at P5 Workshop on the Future of High Energy Physics, BNL, USA, Dec. 15-18, 2013.
URL http://cds.cern.ch/record/2206376

[2] J. Tang, et al., Concept for a Future Super Proton-Proton Collider (2015). arXiv:1507.03224.

[3] R. Calkins, et al., Reconstructing top quarks at the upgraded LHC and at future accelerators, in: Proceedings, Community Summer Study 2013: Snowmass on the Mississippi (CSS2013): Minneapolis, MN, USA, July 29-August 6, 2013. arXiv:1307.6908.
URL https://inspirehep.net/record/1244676/files/arXiv:1307.6908.pdf

[4] S. V. Chekanov, J. Dull, Energy range of hadronic calorimeter towers and cells for high-pT jets at a 100 TeV colliderarXiv:1511.01468.

[5] E. Coleman, M. Freytsis, A. Hinzmann, M. Narain, J. Thaler, N. Tran, C. Vernieri, The importance of calorimetry for highly-boosted jet substructurearXiv:1709.08705.

[6] DELPHES 3 Collaboration, J. de Favereau, C. Delaere, P. Demin, A. Giammanco, V. Lematre, A. Mertens, M. Selvaggi, DELPHES 3, A modular framework for fast simulation of a generic collider experiment, JHEP 02 (2014) 057. arXiv:1307.6346, doi:10.1007/JHEP02(2014)057.

[7] S. V. Chekanov, M. Beydler, A. V. Kotwal, L. Gray, S. Sen, N. V. Tran, S. S. Yu, J. Zuzelski, Initial performance studies of a general-purpose detector for multi-TeV physics at a 100 TeV pp collider, JINST 12 (06) (2017) P06009. arXiv:1612.07291, doi:10.1088/1748-0221/12/06/P06009.

[8] J. Allison, et al., Recent developments in Geant4, Nuclear Instruments and Methods in Physics Research A 835 (2016) 186.

[9] M. J. Charles, PFA Performance for SiD, in: Linear colliders. Proceedings, International Linear Collider Workshop, LCWS08, and International Linear Collider Meeting, ILC08, Chicago, USA, Novermber 16-20, 2008 , 2009. arXiv:0901.4670.

[10] J. S. Marshall, M. A. Thomson, Pandora Particle Flow Algorithm, in: Proceedings, International Conference on Calorimetry for the High Energy Frontier (CHEF 2013), 2013, pp. 305–315. arXiv:1308.4537.

[11] G. P. S. M. Cacciari, G. Soyez, FastJet user manual CERN-PH-TH/2011-297. arXiv:1111.6097.

[12] M. Cacciari, G. P. Salam, G. Soyez, The anti-kt jet clustering algorithm, JHEP 0804 (2008) 063. arXiv:0802.1189.

[13] S. Chekanov, HepSim: a repository with predictions for high-energy physics experiments, Advances in High Energy Physics 2015 (2015) 136093, available as http://atlaswww.hep.anl.gov/hepsim/.

[14] B. Auerbach, S. Chekanov, J. Love, J. Proudfoot, A. Kotwal, Sensitivity to new high-mass states decaying to ttbar at a 100 TeV collider arXiv:1412.5951.

[15] J. Butterworth, B. Cox, J. R. Forshaw, WW scattering at the CERN LHC, Phys.Rev. D65 (2002) 096014. arXiv:hep-ph/0201098, doi:10.1103/PhysRevD.65.096014.

[16] S. Catani, Y. L. Dokshitzer, M. H. Seymour, B. R. Webber, Longitudinally-invariant k-clustering algorithms for hadron-hadron collisions, Nuclear Physics B 406 (12) (1993) 187 – 224.
URL http://www.sciencedirect.com/science/article/pii/055032139390166M

[17] S. D. Ellis, D. E. Soper, Successive combination jet algorithm for hadron collisions, Phys. Rev. D48 (1993) 3160–3166. arXiv:hep-ph/9305266, doi:10.1103/PhysRevD.48.3160.

[18] ATLAS Collaboration Collaboration, G. Aad, et al., Jet mass and substructure of inclusive jets in $\sqrt{s} = 7$ TeV pp collisions with the ATLAS experiment, JHEP 1205 (2012) 128. arXiv:1203.4606, doi:10.1007/JHEP05(2012)128.

[19] J. Thaler, K. Van Tilburg, Identifying Boosted Objects with N-subjettiness, JHEP 03 (2011) 015. arXiv:1011.2268, doi:10.1007/JHEP03(2011)015.